ACCEPTED ARTICLE PREVIEW

**Accepted Article Preview: Published ahead of advance online publication**

# Laser-nanoprinting-enabled multilevel nanoscale phase encoding on quartz for integrated optical diffractive devices

Haitao Luan, Youtao Xing, Yuchi Bai, Yibo Dong and Min Gu

Cite this article as: Haitao Luan, Youtao Xing, Yuchi Bai, Yibo Dong, Min Gu. Laser-nanoprinting-enabled multilevel nanoscale phase encoding on quartz for integrated optical diffractive devices. *Light: Advanced Manufacturing* accepted article preview 9 Febraury, 2026; doi: 10.37188/lam.2026.031

This is a PDF file of an unedited peer-reviewed manuscript that has been accepted for publication. LAM are providing this early version of the manuscript as a service to our customers. The manuscript will undergo copyediting, typesetting and a proof review before it is published in its final form. Please note that during the production process errors may be discovered which could affect the content, and all legal disclaimers apply.

Received 26 June 2025; revised 22 January 2026; accepted 3 Febraury 2026; Accepted article preview online 9 Febraury 2026

Accepted Manuscript

ACCEPTED ARTICLE PREVIEW

# Laser-nanoprinting-enabled multilevel nanoscale phase encoding on quartz for integrated optical diffractive devices

Haitao Luan[1,2]*, Youtao Xing[1,2], Yuchi Bai[1,2], Yibo Dong[1,2]*, Min Gu[1,2]*

[1]School of Artificial Intelligence Science and Technology, University of Shanghai for Science and Technology, Shanghai, 200093, China

[2]Institute of Photonic Chips, University of Shanghai for Science and Technology, Shanghai, 200093, China

*E-mail: haitaoluan@usst.edu.cn; dyb@usst.edu.cn; gumin@usst.edu.cn

## Abstract

To overcome the resolution and stability limitations of conventional grayscale lithography, we present a laser-nanoprinting-assisted technique for multilevel nanoscale phase encoding on a quartz substrate. The proposed approach combines femtosecond laser-based grayscale mask fabrication with multiparameter dry etching optimisation to achieve precise phase modulation with subwavelength resolution approximately 81 nm) and pixel sizes as small as 1 μm$^2$. Up to eight discrete phase levels are supported, enabling efficient diffraction control and device-level functionality. Using this method, various integrated diffractive devices, including lenses, holograms, and diffractive neural networks (DNNs), were realised on quartz substrates. The fabricated structures exhibit high pattern fidelity, mechanical and chemical robustness, and compatibility with standard photonic integration platforms. Notably, a single-layer quartz-based DNN achieved a classification accuracy of 91.75% across four classes of handwritten digits. This nanoprinting-enabled strategy provides a scalable and stable pathway for fabricating compact, multifunctional, and high-resolution diffractive photonic devices.

**Keywords**: Laser-nanoprinting, Grayscale lithography, Dry etching, Diffractive elements, Diffractive neural networks

Accepted Manuscript

ACCEPTED ARTICLE PREVIEW

28 ## Introduction

29 In the past decade, optical information processing has garnered significant
30 interest owing to its superior speed and energy efficiency compared to conventional
31 electronic systems[1-3]. Diffractive optics play a central role in this field, enabling
32 applications such as optical neural networks (ONNs)[4-6], holography[7,8], information
33 encryption[9,10], and optical communications[11,12]. To facilitate practical deployment and
34 chip-level integration, the development of planar diffractive optical elements (DOEs)
35 with nanoscale resolution has become a key research priority. In the visible spectrum,
36 planar DOEs are typically implemented as diffractive surfaces or metasurfaces[13].
37 Diffractive surfaces modulate the optical phase through variations in pixel height or
38 refractive index[14,15]. Compared to metasurfaces, which rely on geometric or
39 resonance-based phase control[16], diffractive surfaces exhibit advantages[13] such as
40 reduced transmission loss, lower fabrication cost, simplified fabrication process, and
41 broader spectral compatibility.

42 Among the various approaches for realising diffractive surfaces, pixel-height
43 modulation via grayscale lithography is particularly attractive owing to its simplicity
44 and compatibility. This enables the construction of multilevel structures by
45 modulating the exposure dose[17-19], employing multiple exposures[20], or adopting
46 three-dimensional (3D) printing techniques[14,21]. In particular, laser-based 3D printing
47 directly produces grayscale patterns through multiphoton polymerisation of
48 photoresists[22,23]. Further integration with galvanometer scanning or projection systems
49 significantly increases the fabrication speed[21,24], positioning this method as a
50 mainstream solution for visible-range diffractive optics.

51 However, existing grayscale lithography techniques face persistent challenges
52 related to resolution and structural reliability. Photoresist-based structures are
53 inherently unstable and susceptible to degradation, which hinders their long-term use
54 in optical systems. To address this, photoresists are often employed as grayscale
55 masks to transfer patterns onto more robust materials, such as $SiO_2$, silicon, or



Accepted Manuscript

ACCEPTED ARTICLE PREVIEW

56 sapphire, via plasma dry etching[18,25-28]. Nonetheless, previous attempts with
57 laser-printed photoresist masks primarily yielded simple structures such as lenses[25]
58 and gratings[29]. Consequently, current grayscale lithography techniques for robust
59 materials fail to meet the increasing demands of complex, high-resolution diffractive
60 surfaces required for advanced applications such as ONNs and holography. A key
61 limitation is the insufficient lateral resolution of the photoresist masks, typically of the
62 order of several tens of microns[25-28], which makes it difficult to realise diffractive
63 features with pixel sizes approaching the visible working wavelengths. In addition,
64 the lack of optimisation of the etching process for anisotropic etching hinders the
65 high-fidelity transfer of grayscale patterns from the photoresist to the substrate.
66 Finally, complex diffractive surfaces require precise phase modulation, which further
67 increases the requirement for etching-rate stability throughout the fabrication process.

68 To overcome these limitations, we present a high-precision grayscale patterning
69 technique that combines ultrahigh-resolution mask fabrication with a finely tuned dry
70 etching process for a quartz substrate (Figs. 1a–c). High-resolution grayscale
71 photoresist masks are fabricated using femtosecond laser-nanoprinting. Fine pattern
72 transfer onto the substrates is achieved through combined multiparameter
73 optimisation of the dry etching process, with key parameters, including gas
74 composition, power, and pressure, which must be carefully tuned. This approach
75 achieves pattern transfer at a resolution of approximately 81 nm and supports eight
76 discrete phase levels with 1 $\mu m^2$ pixel sizes. Representative grayscale patterns such as
77 a "Chinese dragon" and a "flower" were successfully fabricated with nanoscale
78 fidelity (Figs. 1d-e). The number of phase modulation levels plays a critical role in
79 diffractive performance. Notably, increasing the number of grayscale levels
80 significantly enhances the diffraction efficiency, as demonstrated using blazed
81 gratings (Fig. 1f). Moreover, the use of quartz substrates ensures exceptional thermal
82 and mechanical stability, making the structures suitable for practical integration.
83 Importantly, this technique is not limited to quartz and is compatible with silicon



Accepted Manuscript

ACCEPTED ARTICLE PREVIEW

84 wafers, thereby extending its applicability to both optical and electronic devices.
85 Based on this method, we further demonstrate diffractive surfaces with complex phase
86 distributions, such as multilevel holograms, lenses, and DNNs. Notably, the fabricated
87 DNN achieves a classification accuracy of 91.75% on a four-class MNIST dataset.
88 These results represent a substantial advancement toward scalable, high-fidelity, and
89 durable fabrication of multifunctional diffractive optical devices.
90

91 **Etching process optimization for grayscale pattern transfer**

92 Grayscale etching on quartz substrates differs fundamentally from conventional
93 etching methods. In this process, the photoresist mask must be completely removed to
94 ensure a successful grayscale pattern transfer to the substrate. The diffractive surface
95 achieves transmission-type phase modulation by controlling the pixel height[5]. At
96 different operating wavelengths, each pixel requires a specific etching depth to
97 achieve accurate multilevel phase modulation. Therefore, accurate pattern transfer and
98 uniform etching rates for both the photoresist and the substrate must be achieved
99 through the etching process. In the mask-printing stage, a high-resolution photoresist
100 (IP-dip) and a high numerical aperture objective (Plan-Apochromat 63x/1.40 Oil DIC,
101 Zeiss) were employed to obtain nanoscale-resolution masks. Two-photon
102 polymerisation enables mask fabrication with nanoscale resolution beyond the
103 diffraction limit, thereby providing a critical foundation for high-precision etching.
104 Subsequently, the etching parameters were systematically optimised to enable
105 high-precision pattern transfer onto a quartz substrate (Fig. 2).

106 To achieve high-fidelity pattern transfer, it is critical to suppress lateral etching of
107 the photoresist mask. The dry etching process employs inductively coupled plasma
108 reactive ion etching (ICP-RIE), where chemically reactive species generated by gas
109 ionisation react with the substrate, while ion bombardment induces physical
110 reactions[30]. Therefore, the etching process involves both physical and chemical
111 mechanisms.



Accepted Manuscript

ACCEPTED ARTICLE PREVIEW

112 Chemical etching, which is mainly governed by the gas composition, is typically
113 isotropic and is primarily responsible for the lateral etching of the photoresist.
114 Therefore, we investigated the effects of different etching gases—$SF_6$, $CHF_3$, and
115 $CF_4$—on the overall etching performance. Fig. 2a shows the etching selectivity
116 between quartz and photoresist. The etching selectivity, $R=S_{quartz}/S_{photoresist}$, is defined
117 as the ratio of the etching rate of quartz ($S_{quartz}$) to that of the photoresist mask
118 ($S_{photoresist}$). The etching rates of the quartz and photoresist were obtained by measuring
119 their respective etching depths over a specified period using a step profiler and then
120 dividing by the etching time (Methods). Note that $CHF_3$ exhibits a smaller error bar in
121 the etching selectivity between quartz and photoresist, indicating improved etching
122 rate stability. More importantly, $CHF_3$ yields distinct etching selectivity, primarily
123 because of its reduced photoresist etching rate. The measured photoresist etching rates
124 were approximately 563 nmmin$^{-1}$ ($SF_6$+$O_2$), 165 nmmin$^{-1}$ ($CHF_3$+$O_2$), and
125 843 nmmin$^{-1}$ ($CF_4$+$O_2$). This lower etching rate is likely attributable to the reduced
126 fluorine content of $CHF_3$[31]. Consequently, achieving the same substrate-etching depth
127 as $CHF_3$ requires a thinner photoresist mask, which helps reduce the lateral etching of
128 the photoresist mask and enables finer pattern transfer. The error bars were
129 determined by measurements taken at multiple positions across a 2.5 cm × 2.5 cm
130 sample. Before each experiment, we performed equipment ambientization to maintain
131 consistency across different runs. The addition of oxygen helps stabilise the
132 photoresist etching process. The oxygen plasma participates in chemical etching,
133 leading to a more uniform removal rate. In contrast, without oxygen, the photoresist is
134 thinned mainly by physical ion bombardment, which can induce surface
135 cross-linking[32] and cause variations in the etching rate during processing. As shown in
136 Fig. S1, the introduction of oxygen significantly improves the stability of the
137 photoresist etching rate, resulting in a more consistent etching selectivity between
138 quartz and photoresist.

Accepted Manuscript

ACCEPTED ARTICLE PREVIEW

139 In addition to gas composition, both the ICP and radio frequency (RF) powers
140 significantly influence the stability and quality of the etching process (Figs. 2b and c).
141 Within an optimal range, increasing both the ICP and RF powers enhances the etching
142 rate and the etching rate stability. A higher etching rate helps shorten the total etching
143 time, thereby minimising substrate heating, which can otherwise degrade speed
144 stability[33,34]. An ICP power of 1200 W and an RF power of 100 W yielded the best
145 results; beyond this, the performance declined owing to power instability. Moreover,
146 more surface defects were observed at lower RF power (Fig. S 2). The chamber
147 pressure is another critical parameter. The patterns transferred after etching under low
148 pressure had lower fidelity (Fig. S3). At a pressure of 20 mTorr, the etching process
149 exhibited an improved etching rate stability (Fig. 2d) and yielded surfaces with
150 minimal defects (Fig. S4). These findings highlight the necessity of coordinated
151 multiparameter optimisation for stable and precise grayscale pattern transfer.

152 Following this optimisation, stable etching rates were achieved for both quartz
153 substrates and photoresist masks, with a final etching selectivity of $R = 0.43$. The
154 etching parameters were finally set as follows: $SF_6/O_2$ = 40/10 sccm, ICP power =
155 1200 W, RF power = 100 W, and chamber pressure = 20 mTorr. Using these
156 optimised parameters, we achieved a minimum feature lateral linewidth of 81 nm on
157 the quartz substrate (Fig. 2e), whereas the corresponding photoresist mask exhibited a
158 linewidth of approximately 100 nm. The deviation between the mask and quartz
159 linewidths primarily originates from lateral etching during the dry-etching process. As
160 discussed earlier, the chemical reactions involved in plasma etching are typically
161 isotropic and contribute to etching in all directions. Although this effect was
162 suppressed through multiparameter optimisation, a certain degree of lateral etching
163 remains, resulting in a reduced final linewidth compared to that of the photoresist
164 mask. Because both the photoresist mask fabrication and dry-etching processes are
165 isotropic in the x- and y-directions, the achieved lateral resolution of 81 nm applies
166 equally along both axes. Fig. S5 shows the etching results for different values of
167 lateral linewidth and line spacing.

Accepted Manuscript

ACCEPTED ARTICLE PREVIEW

168 For comparison, Fig. 2f presents scanning electron microscopy (SEM) images of 169 grayscale patterns etched with a pixel size of 1 $\mu m^2$ using unoptimised empirical 170 parameters—originally developed for standard $SiO_2$ films in our laboratory—and 171 those obtained under optimised etching conditions. The results highlight a substantial 172 improvement in pattern fidelity. Lateral etching persisted after optimisation, as 173 evidenced by the tilted SEM images (Fig. S6). Nevertheless, by comparing the degree 174 of lateral etching before and after optimisation, it can be seen that lateral etching was 175 greatly reduced (Fig. S7).

176 Moreover, this technique is compatible with silicon wafers, as shown in Fig. S8. 177 While our main focus is on quartz substrates for diffractive surface fabrication, we 178 further investigated and optimised etching parameters on silicon to extend the scope 179 of this approach. The results demonstrate that beyond diffractive optics, the method 180 can be applied to silicon-based grayscale patterning, highlighting its potential for 181 integrated photonic and electronic devices.

182 **Diffractive surfaces fabrication for hologram and lens**

183 High-precision functional diffractive surfaces were fabricated on quartz 184 substrates to demonstrate the versatility of the proposed technique. As a representative 185 sample, an 8-level phase-modulated hologram (100×100 pixels with a pixel size of 186 1 $\mu m^2$) was designed using the Gerchberg–Saxton algorithm[35] to reconstruct the letters 187 "IPC" (Institute of Photonic Chips). We selected 8-level phase modulation for two 188 reasons. First, laser-printed masks employ a piezoelectric displacement stage for 189 grayscale height control. Although the stage provides ±10 nm displacement 190 accuracy—sufficient for higher-order grayscale masks—additional levels would 191 substantially increase fabrication time. Second, as shown in Fig. 1f, 8-level phase 192 modulation already achieves high diffraction efficiency for diffractive elements, 193 meeting the requirements of holographic displays and representing a widely adopted 194 standard in diffractive optics[36-38]. With this choice, the entire fabrication process, 195 including both laser-nanoprinting and dry etching, was completed in less than 20 min, 196 with the laser printing step requiring only approximately 2 min.



Accepted Manuscript

ACCEPTED ARTICLE PREVIEW

197 For a working wavelength of 532 nm, the required etching depths for each phase
198 level were calculated using the equation $\varphi(\lambda) = 2\pi(n - 1)h/\lambda$[5,7], where $\varphi(\lambda)$ is the
199 phase shift at wavelength $\lambda$, $n$ is the refractive index of quartz (approximately 1.5),
200 and $h$ is the etching depth. These calculations were matched with the experimentally
201 determined etching selectivity ($R$) to define the corresponding height of the
202 photoresist mask. Fig. 3a illustrates the optical setup used for holographic testing. For
203 comparison, a hologram with the same design was fabricated directly on the
204 photoresist. Owing to the similar refractive indices of IP-Dip and quartz, the atomic
205 force microscopy (AFM) measurements showed that the two structures exhibited
206 comparable feature heights (Fig. S9). It should be noted that, owing to the principle of
207 two-photon polymerization[22], the effective exposure volume is confined to the focal
208 region of the objective, producing an ellipsoidal solidified structure with intrinsically
209 rounded edges. The AFM images reveal that the mask pixels possess smooth edge
210 profiles.

211 Fig. 3b shows that the measured average step height between adjacent phase
212 levels was approximately 132.53 nm, which confirms the agreement between
213 measured and designed etching depths, supporting the accuracy of the fabrication
214 process. Although lateral etching was effectively suppressed, minor surface
215 nonuniformities were still observed; thus, the etching depth data in Fig. 3b were
216 obtained primarily from the central regions of the pixels to ensure measurement
217 consistency. The final morphology of the hologram is shown in Fig. 3c, demonstrating
218 high structural fidelity.

219 The quartz-based diffractive surface exhibited superior stability under extreme
220 environmental conditions. To assess thermal robustness, both the quartz and
221 photoresist-based holograms were subjected to annealing. As shown in Fig. 3d, the
222 initial display quality and peak signal-to-noise ratio (PSNR) were higher for the
223 photoresist hologram. However, following thermal treatment at 400 °C, the
224 photoresist hologram exhibited significant structural degradation, whereas the



Accepted Manuscript

ACCEPTED ARTICLE PREVIEW

225 quartz-based structure remained intact. This observation was confirmed by the SEM
226 images shown in Fig. 3e. The PSNR values of the holographic images before and after
227 annealing were calculated (Fig. S10). In addition, the chemical resistance was
228 evaluated via acid treatment, and the quartz-based hologram showed no apparent
229 damage (Fig. S11), which further demonstrates its environmental durability.

230 A diffractive lens with a focal length of 500 μm was also fabricated to validate
231 the general applicability of the technique. As shown in Fig. 3f, the fabricated phase
232 profile closely matched the design target. Optical characterisation showed that the
233 lens successfully focused incident light at the intended distance of approximately
234 500 μm, consistent with the theoretical predictions of lens performance (Fig. 3g). The
235 diffraction efficiency measured using a beam profiler was approximately 71% (Fig.
236 S12). This is slightly lower than the theoretical value of 86.08%, with the discrepancy
237 primarily attributed to fabrication inaccuracies, namely the resolution limit of the
238 laser-printed mask and lateral etching effects during the grayscale pattern transfer.

239

240 **Diffractive surfaces fabrication for diffractive neural networks**

241 ONNs, which use light as an information carrier, have attracted significant
242 research interest owing to their ultralow energy consumption and ultrahigh processing
243 speed[2,3]. Among various ONN architectures, DNNs, a class of free-space ONNs, stand
244 out for their high-throughput computational capabilities[4,39,40]. As illustrated in Fig. 4a,
245 DNNs modulate light fields through phase-encoded neurons, whereas the weighted
246 multiplication and summation operations between neurons are implemented via
247 optical diffraction and coherent interference. Owing to their inherent 3D architecture,
248 laser-nanoprinting has emerged as a widely used method for DNNs[4,14,41]. However,
249 existing implementations based on photoresist structures have limitations in terms of
250 their long-term reliability, particularly under thermal or chemical stress.

251 In this study, we demonstrate the fabrication of a single-layer DNN (100×100
252 pixels with a pixel size of 1 μm$^2$) directly on a quartz substrate using this technique.



Accepted Manuscript

ACCEPTED ARTICLE PREVIEW

253 The DNN was trained on the MNIST dataset, which comprises 2,000 images (500 per
254 class), using Google TensorFlow 2.6.0. The phase profile of the diffractive layer was
255 optimised using back-propagation and gradient descent (Fig. S13a). To enhance
256 performance, the propagation distance between the input and output layers was
257 optimised based on the Fresnel number[42], achieving a training accuracy of 96.6% (Fig.
258 S13b). Fig. 4b presents the resulting phase distribution and fabricated DNN surface
259 morphology. The optical setup is shown in Fig. 4c. Input patterns[43] were encoded
260 using a spatial light modulator (SLM), in combination with a quarter-wave plate
261 (QWP) and a polariser. By appropriately selecting the fast-axis angle of the QWP,
262 orientation of the polariser, and phase setting of the SLM, this configuration enables
263 amplitude-based image encoding without introducing additional phase profiles (Fig.
264 S14 and Note 1). Consequently, the potential phase noise in the input images is
265 reduced, which has been demonstrated to negatively affect the recognition
266 performance of DNNs[44]. The output patterns were captured using a charge-coupled
267 device (CCD) camera placed downstream of the DNN and aligned in a 4f optical
268 configuration. Representative input images and corresponding output results for
269 handwritten digits are shown in Fig. 4d. For each input digit, the correct detection
270 region among the four white dashed circles exhibited the highest intensity, indicating
271 successful classification by the DNN. The DNN was evaluated using 400 test images
272 (100 images from each category). The confusion matrix shown in Fig. 4e reveals that
273 the DNN achieves a classification accuracy of 91.75%, thus confirming the
274 effectiveness of the diffractive structure. It should be noted that the DNN can, in
275 principle, support more classification categories, but its accuracy decreases
276 significantly (Fig. S15a). Thus, in addition to increasing the number of diffractive
277 layers, the simulations suggest that increasing the pixel count within each layer can
278 provide notable performance gains (Fig. S15b). Increasing the number of pixels
279 requires enlarging the printed etching-mask area. A practical approach is to divide a
280 large etching mask into multiple subregions and print them sequentially.



Accepted Manuscript

ACCEPTED ARTICLE PREVIEW

281

282 In summary, we developed a laser-nanoprinting-based grayscale lithography 283 technique combined with multiparameter etching optimisation to achieve 284 high-precision pattern transfer onto a quartz substrate. This approach enabled the 285 fabrication of multilevel diffractive surfaces with nanoscale resolution (~81 nm), 286 supporting eight discrete phase levels within 1 μm² pixels. Compared to conventional 287 grayscale lithography, the proposed method overcomes critical resolution limitations 288 and improves long-term material stability. Its effectiveness has been validated by the 289 successful realisation of functional diffractive devices, including holograms and 290 diffractive neural networks. The fabricated surfaces exhibit lateral dimensions down 291 to 100 μm, high structural fidelity, and operational durability, thereby addressing key 292 demands in the development of compact, reliable, and highly integrated photonic 293 systems. To further improve the grayscale patterning resolution, future work may 294 involve the adoption of two-beam laser writing techniques[22,45,46], which offer 295 enhanced spatial control and mask definition.

296 Compared with photoresists, quartz and silicon exhibit much higher mechanical 297 strength and chemical stability, ensuring superior durability and reliability. Therefore, 298 diffractive structures fabricated on these substrates can operate stably under diverse 299 conditions, including extreme environments such as strong radiation, high 300 temperatures, and deep-sea and deep-space settings. Consequently, the proposed 301 method offers enhanced flexibility and broader practical potential than 302 photoresist-based approaches.

303 In terms of specific applications, the demonstrated technique is particularly 304 promising for integrated photonic systems, except for conventional diffractive 305 elements such as holograms and lenses. The use of quartz or Si substrates offers 306 enhanced structural robustness and integration compatibility. This enables monolithic 307 integration of diffractive surfaces with a wide range of nano- and micro-scale optical 308 components. For instance, they can be directly implemented on optical fibre end faces



Accepted Manuscript

ACCEPTED ARTICLE PREVIEW

309 for beam modulation[47] and in-fibre imaging[6], or integrated with light sources such as
310 vertical-cavity surface-emitting lasers for applications such as vortex beam
311 generation[21,48] and holography[49]. This level of compatibility facilitates the
312 development of compact actively modulated photonic devices. To further broaden
313 their applicability, we investigated and optimised the etching parameters for silicon
314 wafers, thereby extending this technique to a wider set of platforms. Overall, the
315 demonstrated technique provides a versatile platform for the fabrication of
316 high-resolution diffractive structures with potential applications in integrated
317 photonics, optical computing, and optoelectronic systems.

318

319 ## Methods

320 **Laser-nanoprinting of etching masks**

321 The fabrication process for diffractive surfaces on a quartz substrate is illustrated
322 in Fig. 1b. First, the etching masks were printed using a commercial two-photon
323 lithography system (Photonic Professional GT, Nanoscribe GmbH), equipped with a
324 780 nm, 80 MHz femtosecond laser. This system includes a high-numerical-aperture
325 immersion objective (Plan-Apochromat 63×/1.40 oil phase contrast, Zeiss) in the
326 galvanometer scanning mode. A two-photon photoresist (IP-Dip) was used as the
327 printing material. Commercial 1-inch quartz substrates (thickness: 0.5 mm) were used.
328 The diffractive phase plates were designed with a resolution of 100 × 100 pixels and a
329 pixel area of 1 $\mu m^2$. Based on the experimentally determined etching selectivity, the
330 hatching distance was set to 0.05 µm, and the height gradient of the photoresist mask
331 was set to 0.306 µm. After etching, this yielded diffractive surfaces with a height
332 gradient of approximately 0.133 µm, corresponding to a phase modulation of ¼π at a
333 working wavelength of 532 nm. The optimised laser power and scanning speed were
334 18 mW and 10,000 $\mu m s^{-1}$, respectively. After laser printing, the samples were
335 developed in propylene glycol methyl ether acetate for 25 min, rinsed with
336 isopropanol for 5 min, and then dried.



Accepted Manuscript

ACCEPTED ARTICLE PREVIEW

337 **Grayscale etching of quartz**

338 Grayscale pattern transfer onto the quartz substrate was achieved by fully etching
339 the photoresist mask using an Oxford etching system (Plasmalab System 100, Oxford
340 Instruments). To ensure process stability, a 6-inch Si wafer was initially placed in the
341 etching chamber and cleaned with oxygen plasma for 30 min. A 15-min
342 ambientization step was then performed to confirm the chamber cleanliness using the
343 same parameters as those employed in the real etching process.

344 During etching, the quartz substrate was bonded to a Si wafer using thermal
345 grease to prevent excessive heating. The etching parameters were as follows: $CHF_3$
346 flow rate, 40 sccm; $O_2$ flow rate, 10 sccm; ICP power, 1200 W; RF power, 100 W; and
347 chamber pressure, 20 mTorr. After etching, the samples were ultrasonically cleaned
348 with ethanol for 30 min.

349 When characterising the etching selectivity shown in Fig. 2, the etching rates of
350 the quartz and photoresist were determined by measuring their etching depths over a
351 specified time period using a step profiler and dividing the measured depth by the
352 etching duration. First, the initial thickness of the photoresist mask ($d_{photoresist}$) was
353 measured. After etching for a specified time $t$ while a portion of the photoresist mask
354 remained, the total height of the etched structure ($d_1$) was measured. At this stage,
355 $d_1=d_{photoresist}'+d_{quartz}$, where $d_{photoresist}'$ is the remaining photoresist thickness after
356 etching, and $d_{quartz}$ is the etching depth of quartz. The photoresist was then removed
357 and the quartz etching depth $d_{quartz}$ was directly measured using the step profiler.
358 Accordingly, the quartz etching rate is $S_{quartz}=d_{quartz}/t$, and the photoresist etching rate
359 is $S_{photoresist}=(d_{photoresist}-d_{photoresist}')/t=(d_{photoresist}-d_1+d_{quartz})/t$.

360 **Optical setups and characterization for diffractive surfaces**

361 A 532 nm solid-state laser was used as the light source for all optical
362 characterisations. A 4f optical system was used to control the beam diameter. For
363 hologram testing, the laser beam was directed onto the hologram using an additional
364 lens (L4 in Fig. 3a), which focused the beam and performed the Fourier transform.



Accepted Manuscript

ACCEPTED ARTICLE PREVIEW

365 An auxiliary imaging path composed of an illumination source and lenses was
366 incorporated to ensure precise spatial alignment between the incident beam and the
367 hologram.

368 For DNN testing, an SLM (EXULUS-HD2, Thorlabs) was introduced into the
369 optical path. This configuration enabled the generation of amplitude-modulated input
370 signals in conjunction with a quarter-wave plate and polariser (Supplementary Note 1).
371 The DNN sample was positioned between the two objective lenses (L3 and L4 in
372 Fig. 4c), forming a 4f system for testing. All output signals were captured using a
373 CCD camera.

374 For structural characterisation, SEM images were acquired using a ZEISS Sigma
375 300 microscope, and AFM measurements were performed using a Bruker Dimension
376 Icon system.

377 **DNN Training**

378 DNN training was performed using TensorFlow 2.6.0. The input images from the
379 MNIST dataset were resized to $100 \times 100$ pixels to match the network dimensions.
380 The forward propagation of the optical field was simulated using the angular spectrum
381 method to account for light diffraction[50]. A cross-entropy loss function was defined
382 based on the predicted outputs and true labels. The phase distribution of the
383 diffractive layer was iteratively optimised using backpropagation and gradient descent.
384 To enhance performance, the distances from the input and output layers to the
385 diffractive layer were optimised based on the Fresnel number, and set to 1900 μm and
386 6600 μm, respectively. The training was conducted during 300 epochs with a learning
387 rate of 0.03.

388 **Calculation of diffraction efficiency of gratings**

389 The diffraction efficiency shown in Fig. 1f was calculated based on the Fourier
390 theory (scalar diffraction theory)[51], the core of which is to expand the transmission
391 function of the periodic step structure of the element into a Fourier series and obtain



Accepted Manuscript

ACCEPTED ARTICLE PREVIEW

392 the sub-efficiency of each diffraction level by squaring the coefficients. For blazed
393 gratings, the $n$-order diffraction efficiency is given by

$$\eta_n = \left[\frac{\sin(\pi n / N)}{\pi n / N}\right]^2$$

394 where $N$ is the number of steps.
395

396 **Acknowledgements**

397 We acknowledge the support from the National Key Research and Development
398 Program of China (2022YFB2804301), the Science and Technology Commission of
399 Shanghai Municipality (Grant No. 21DZ1100500), the Shanghai Municipal Science
400 and Technology Major Project, the Shanghai Frontiers Science Center Program
401 (2021–2025 No. 20), and the Shanghai Sailing Program (23YF1429500).
402

403 **Data availability**

404 Data supporting the findings of this study are available upon request from the
405 corresponding author.
406

407 **Author contributions**

408 H.T.L., Y.B.D., and M.G. conceived the idea. Y.B.D. and M.G. supervised the project.
409 H.T.L. and Y.T.X. performed laser printing, etching, and characterization. H.T.L.,
410 Y.T.X., and Y.C.B. performed the testing of the diffractive surfaces. H.T.L. wrote the
411 first draft of the paper. Y.B.D. and M.G. revised the manuscript.
412

413 **Conflict of interest**

414 The authors declare no competing interests.
415

416 **Additional information**



Accepted Manuscript

ACCEPTED ARTICLE PREVIEW

417 Papers containing Supplementary Information contain the statement:

418 "Supplementary Information is available for this paper."

419

420 **References**


421 1. Shastri, B. J. et al. Principles of neuromorphic photonics. in Unconventional
422 Computing (ed Adamatzky, A.) (New York: Springer, 2018), 83-118.
423 2. Wetzstein, G. et al. Inference in artificial intelligence with deep optics and
424 photonics. *Nature* **588**, 39-47 (2020).
425 3. Shastri, B. J. et al. Photonics for artificial intelligence and neuromorphic
426 computing. *Nature Photonics* **15**, 102-114 (2021).
427 4. Lin, X. et al. All-optical machine learning using diffractive deep neural
428 networks. *Science* **361**, 1004-1008 (2018).
429 5. Dong, Y. B. et al. Compact eternal diffractive neural network chip for extreme
430 environments. *Communications Engineering* **3**, 64 (2024).
431 6. Yu, H. Y. et al. All-optical image transportation through a multimode fibre
432 using a miniaturized diffractive neural network on the distal facet. *Nature*
433 *Photonics* **19**, 486-493 (2025).
434 7. Lim, K. T. et al. Holographic colour prints for enhanced optical security by
435 combined phase and amplitude control. *Nature Communications* **10**, 25
436 (2019).
437 8. Qu, G. Y. et al. Reprogrammable meta-hologram for optical encryption.
438 *Nature Communications* **11**, 5484 (2020).
439 9. Dong, Y. B. et al. Laser-induced graphene hologram reconfiguration for
440 countersurveillance multisecret sharing. *Laser & Photonics Reviews* **17**,
441 2200805 (2023).
442 10. Georgi, P. et al. Optical secret sharing with cascaded metasurface holography.
443 *Science Advances* **7**, eabf9718 (2021).
444 11. Rahman, S. S. et al. Learning diffractive optical communication around
445 arbitrary opaque occlusions. *Nature Communications* **14**, 6830 (2023).
446 12. Chen, Y. T. et al. Photonic unsupervised learning variational autoencoder for
447 high-throughput and low-latency image transmission. *Science Advances* **9**,
448 eadf8437 (2023).
449 13. Hu, J. T. et al. Diffractive optical computing in free space. *Nature*
450 *Communications* **15**, 1525 (2024).
451 14. Goi, E., Schoenhardt, S. & Gu, M. Direct retrieval of Zernike-based pupil
452 functions using integrated diffractive deep neural networks. *Nature*
453 *Communications* **13**, 7531 (2022).


Accepted Manuscript

454 15. Li, X. P. et al. Athermally photoreduced graphene oxides for
455 three-dimensional holographic images. *Nature Communications* **6**, 6984
456 (2015).
457 16. Liu, M. J. et al. Phase modulation mechanism and research progress of
458 multifunctional metasurfaces. *Acta Optica Sinica* **42**, 2126004 (2022).
459 17. Williams, C. et al. Grayscale-to-color: scalable fabrication of custom
460 multispectral filter arrays. *ACS Photonics* **6**, 3132-3141 (2019).
461 18. Aguiam, D. E. et al. Fabrication and optical characterization of large aperture
462 diffractive lenses using greyscale lithography. *Micro and Nano Engineering*
463 **14**, 100111 (2022).
464 19. Abdul Hamid, I. S. L. et al. Implementation of a single emulsion mask for
465 three-dimensional (3D) microstructure fabrication of micromixers using the
466 grayscale photolithography technique. *Micromachines* **11**, 548 (2020).
467 20. Li, X. H., Tan, Z. J. & Fang, N. X. Grayscale stencil lithography for patterning
468 multispectral color filters. *Optica* **7**, 1154-1161 (2020).
469 21. Dong, Y. B. et al. Nanoprinted diffractive layer integrated vertical-cavity
470 surface-emitting vortex lasers with scalable topological charge. *Nano Letters*
471 **23**, 9096-9104 (2023).
472 22. Fischer, J. & Wegener, M. Three-dimensional optical laser lithography beyond
473 the diffraction limit. *Laser & Photonics Reviews* 7, 22-44 (2013).
474 23. Wang, H. et al. Two-photon polymerization lithography for imaging optics.
475 *International Journal of Extreme Manufacturing* **6**, 042002 (2024).
476 24. Somers, P. et al. Rapid, continuous projection multi-photon 3D printing
477 enabled by spatiotemporal focusing of femtosecond pulses. *Light*: *Science &*
478 *Applications* **10**, 199 (2021).
479 25. Liu, X. Q. et al. Ultra-smooth micro-optical components of various geometries.
480 *Optics Letters* **44**, 2454-2457 (2019).
481 26. Khazi, I., Muthiah, U. & Mescheder, U. 3D free forms in c-Si via grayscale
482 lithography and RIE. *Microelectronic Engineering* **193**, 34-40 (2018).
483 27. Cunha, J. et al. Assessing tolerances in direct write laser grayscale lithography
484 and reactive ion etching pattern transfer for fabrication of 2.5D Si master
485 molds. *Micro and Nano Engineering* **19**, 100182 (2023).
486 28. Gurung, S. et al. Phase mask fabrication for multi-plane light conversion using
487 grayscale lithography. Print at https://doi.org/10.48550/arXiv.2507.10405
488 (2025).
489 29. Liu, X. Q. et al. Wear-resistant blazed gratings fabricated by etching-assisted
490 femtosecond laser lithography. *Journal of Lightwave Technology* **39**,
491 4690-4694 (2021).
492 30. Marrian, C. R. K. & Tennant, D. M. Nanofabrication. *Journal of Vacuum*
493 *Science & Technology A* **21**, S207-S215 (2003).

Accepted Manuscript

ACCEPTED ARTICLE PREVIEW


494 31. Donnelly, V. M. & Kornblit, A. Plasma etching: yesterday, today, and
495 tomorrow. *Journal of Vacuum Science & Technology A* **31**, 050825 (2013).
496 32. Dong, Y. B. et al. Metal-catalyst-free growth of patterned graphene on $SiO_2$
497 substrates by annealing plasma-induced cross-linked parylene for
498 optoelectronic device applications. *ACS Applied Materials & Interfaces* **11**,
499 14427-14436 (2019).
500 33. Tesauro, M. R. & Roche, G. In-situ measurement of the relative thermal
501 contributions of chemical reactions and Ions during plasma etching. *ECS*
502 *Transactions* **13**, 3-15 (2008).
503 34. Min, J. H. et al. Redeposition of etch products on sidewalls during $SiO_2$
504 etching in a fluorocarbon plasma. IV. Effects of substrate temperature in a $CF_4$
505 plasma. *Journal of Vacuum Science & Technology B* **21**, 2198-2204 (2003).
506 35. Gerchberg, R. & Saxton, W. A practical algorithm for the determination of
507 phase from image and diffraction plane pictures. *SPIE Milestone Series MS* **94**,
508 646 (1994).
509 36. Huang, K. et al. Silicon multi-meta-holograms for the broadband visible light.
510 *Laser & Photonics Reviews* **10**, 500-509 (2016).
511 37. Lv, Y. et al. Femtosecond laser-induced refractive index modulation of 2D
512 perovskites for phase-modulated holographic neural networks. *ACS Photonics*
513 **12**, 3618-3625 (2025).
514 38. Liu, Z. B. et al. Broadband, low-crosstalk, and massive-channels OAM modes
515 de/multiplexing based on optical diffraction neural network. *Laser &*
516 *Photonics Reviews* **17**, 2200536 (2023).
517 39. Zhou, T. K. et al. Large-scale neuromorphic optoelectronic computing with a
518 reconfigurable diffractive processing unit. *Nature Photonics* **15**, 367-373
519 (2021).
520 40. Liu, C. et al. A programmable diffractive deep neural network based on a
521 digital-coding metasurface array. *Nature Electronics* **5**, 113-122 (2022).
522 41. Chen, H. et al. Superresolution imaging using superoscillatory diffractive
523 neural networks. *Advanced Photonics* **6**, 056004 (2024).
524 42. Zheng, M. J., Shi, L. & Zi, J. Optimize performance of a diffractive neural
525 network by controlling the Fresnel number. *Photonics Research* **10**,
526 2667-2676 (2022).
527 43. Li, Y. Z., Xue, Y. J. & Tian, L. Deep speckle correlation: a deep learning
528 approach toward scalable imaging through scattering media. *Optica* **5**,
529 1181-1190 (2018).
530 44. Dong, Y. B. et al. High-throughput optical neuromorphic graphic processing at
531 millions of images per second. *eLight* **5**, 29 (2025).
532 45. Zhao, M. et al. A 3D nanoscale optical disk memory with petabit capacity.
533 *Nature* **626**, 772-778 (2024).


Accepted Manuscript

ACCEPTED ARTICLE PREVIEW

534 46. Gan, Z. S. et al. Three-dimensional deep sub-diffraction optical beam
535 lithography with 9 nm feature size. *Nature Communications* **4**, 2061 (2013).
536 47. Li, C. H. et al. Metafiber transforming arbitrarily structured light. *Nature*
537 *Communications* **14**, 7222 (2023).
538 48. Li, H. L. et al. Orbital angular momentum vertical-cavity surface-emitting
539 lasers. *Optica* **2**, 547-552 (2015).
540 49. Ni, P. N. et al. Spin-decoupling of vertical cavity surface-emitting lasers with
541 complete phase modulation using on-chip integrated Jones matrix
542 metasurfaces. *Nature Communications* **13**, 7795 (2022).
543 50. Goodman, J. W. Introduction to Fourier Optics. 3rd edn. (Englewood: Roberts
544 & Co., 2005).
545 51. Cox, J. A. et al. Diffraction efficiency of binary optical elements. Proceedings
546 of SPIE 1211, Computer and Optically Formed Holographic Optics. Los
547 Angeles: SPIE, 1990.

548

Accepted Manuscript

549 **Figures**

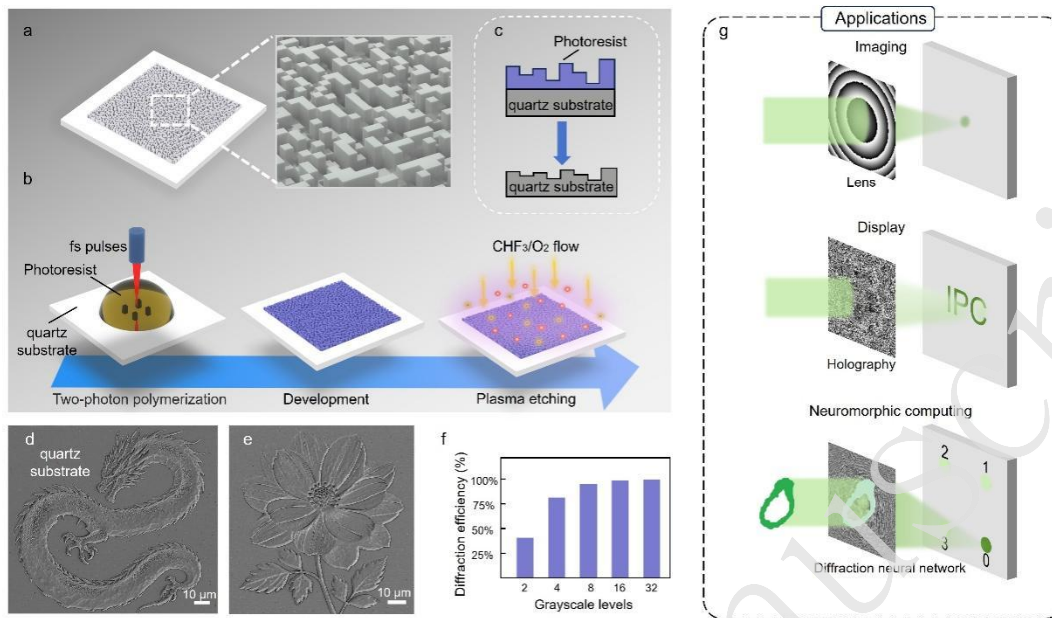


550

551 **Fig. 1.** Principle of the grayscale patterning technique on quartz substrate. **a**,
552 Schematic illustration of the morphology of diffractive surfaces fabricated using the
553 proposed technique. **b**, High-precision grayscale lithography achieved via a
554 single-step lithography and dry etching process. **c**, Schematic of grayscale pattern
555 transfer from the photoresist mask to the substrate through optimized etching. **d, e**,
556 High-resolution grayscale patterns—a "Chinese dragon" and a "flower"—fabricated
557 on quartz substrates. **f**, Calculated 1$^{st}$-order diffraction efficiency of blazed gratings as
558 a function of phase modulation levels, highlighting the advantage of multi-level phase
559 modulation. **g**, Demonstrated applications of the technique, including lenses,
560 holograms, and DNN.

561

562

563

Accepted Manuscript

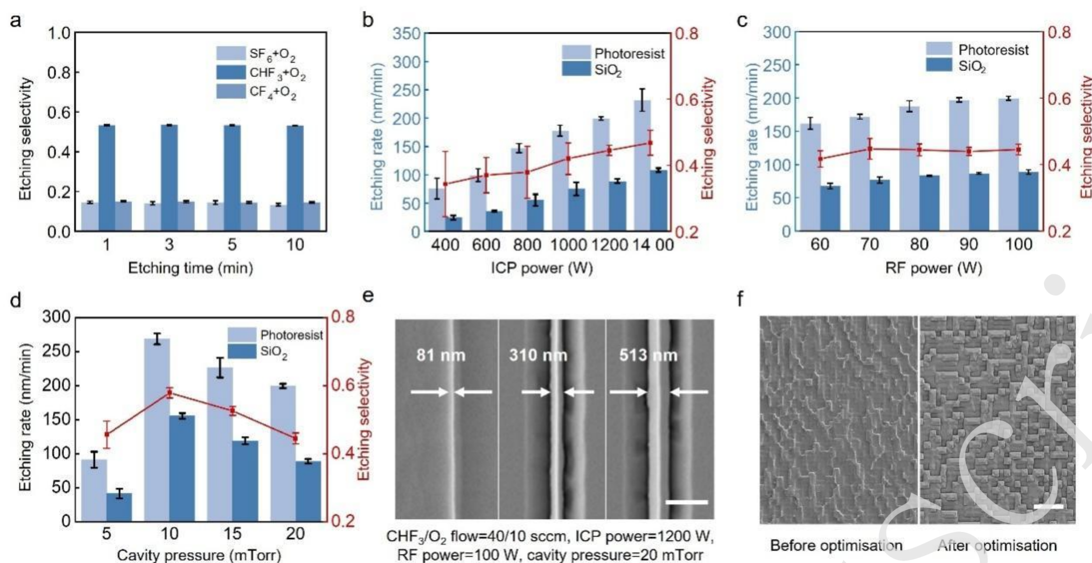


564

565 **Fig. 2.** Multiparameter optimisation of etching conditions for high-precision grayscale
566 pattern transfer on quartz substrate. **a**, Etching selectivity of quartz-to-photoresist as a
567 function of etching time under different gas compositions. The total gas flow rate was
568 maintained at 50 sccm, with $SF_6$, $CHF_3$, and $CF_4$ each at 40 sccm and $O_2$ at 10 sccm. **b**,
569 Etching rate and selectivity as a function of ICP power. **c**, Etching rate and selectivity
570 as a function of RF power. **d**, Etching rate and selectivity as a function of chamber
571 pressure. **e**, SEM images showing different etched lateral line widths achieved using
572 the optimized parameters. Scale bar: 1 μm. **f**, Comparison of SEM images of
573 diffractive surfaces before (using empirical $SiO_2$ etching parameters:
574 $SF_6/O_2$ = 40/10 sccm, ICP = 1000 W, RF = 90 W, pressure = 20 mTorr) and after
575 parameter optimisation, demonstrating enhanced etching fidelity. Scale bar: 5 μm.

576

577

578

579

580

581

582

Accepted Manuscript

ACCEPTED ARTICLE PREVIEW

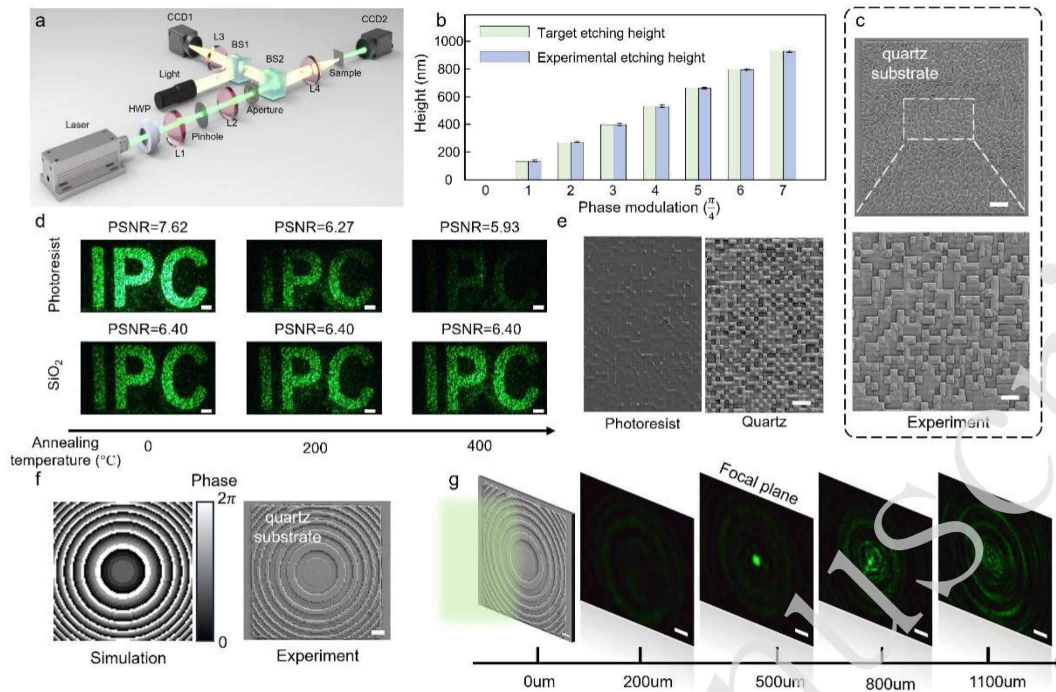


583

584 **Fig. 3.** Quartz-based high-precision diffractive surfaces for holography and lensing. **a**,
585 Optical setup for hologram testing. **b**, Target grayscale etching depths and
586 corresponding experimental results for an 8-level phase modulation diffractive surface
587 working at 532 nm laser. **c**, SEM images of the fabricated hologram at different
588 magnifications. Scale bars: 5 µm (top), 2 µm (bottom). **d**, Holographic images
589 reconstructed from photoresist-based (top) and quartz-based (bottom) holograms after
590 annealing at various temperatures for 30 min. Scale bar: 1 mm. **e**, SEM images of the
591 two holograms after annealing at 400 °C for 30 min. Scale bar: 5 µm. **f**, Calculated
592 phase distribution and corresponding SEM image of the diffractive surface designed
593 for lensing. Scale bar: 10 µm. **g**, Captured intensity profiles of the light field at
594 different propagation distances after transmission through the diffractive lens. Scale
595 bar: 0.1 mm.

596

597

598



Accepted Manuscript

ACCEPTED ARTICLE PREVIEW

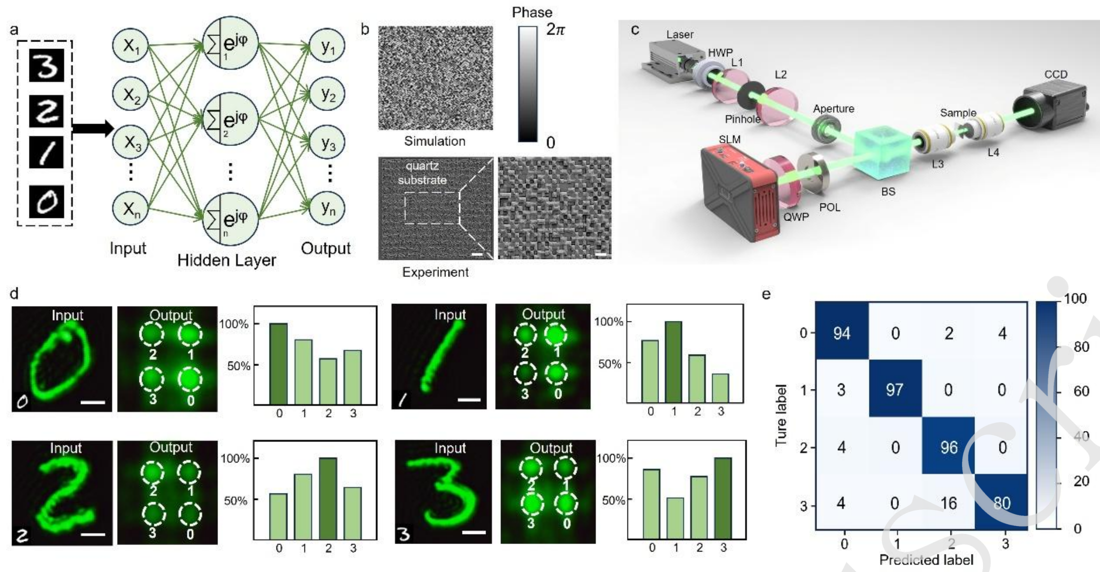


**Fig. 4.** Quartz-based high-precision diffractive surface for DNN application. **a**, Schematic illustration of the mathematical operation flow of the diffractive neural network (DNN). **b**, Phase distribution obtained after training and corresponding SEM images of the fabricated diffractive surface (scale bars: 10 μm and 3 μm). **c**, Optical setup used for DNN testing. **d**, Example input image, resulting output light field, and normalised output intensities corresponding to each detection region; scale bar: 0.1 mm. **e**, Confusion matrix of the DNN for classification results over 400 test images.

Accepted Manuscript